PREPARATION OF FREEZE-CAST SCAFFOLDS FROM 58S AND 13-93 SOL-GEL BIOACTIVE GLASSES FOR BONE TISSUE ENGINEERING APPLICATIONS

Diogo M.M. dos Santos[1,*]; Gustavo L. de Oliveira[1]; Daniel C.F. Soares[2]; Matheus V. Maia[2]; Francesca Tallia[3]; Agathe Heyraud[3]; Julian Jones[3]; Manuel Houmard[4,5]; Eduardo H.M. Nunes[1,5⊥]

1. Universidade Federal de Minas Gerais (UFMG), Departamento de Engenharia Metalúrgica e de Materiais (DEMET), Av. Presidente Antônio Carlos, 6627 – Pampulha, Belo Horizonte – MG, CEP: 31270-901, Brasil.

2. Universidade Federal de Itajubá (UNIFEI), Campus Prof. José Rodrigues Seabra, Av. BPS, 1303 - Bairro Pinheirinho, Itajubá – MG, CEP: 37500 903, Brasil.

3. Imperial College London, Faculty of Engineering, Department of Materials. South Kensington Campus, London SW7 2AZ, England.

4. Universidade Federal de Minas Gerais (UFMG), Departamento de Engenharia Química (DEQ), Av. Presidente Antônio Carlos, 6627 – Pampulha, Belo Horizonte – MG, CEP: 31270-901, Brasil.

5. Centro de Tecnologia em Nanomateriais e Grafeno (CTNano), R. Professor José Vieira de Mendonça, nº 520 – Engenho Nogueira, Belo Horizonte – MG, CEP: 31310-260, Brasil.

ABSTRACT

This study investigates the fabrication of composite scaffolds using 58S and 13-93 bioactive glass particles via freeze casting followed by sintering at 650 °C. The 30/70 mass ratio of 58S/13-93 produced scaffolds with the lowest porosity (70.1 ± 2.4%) and the highest compressive strength (11.25 ± 2.48 MPa). These scaffolds had well-ordered lamellar pores conducive to bone regeneration, as confirmed by scanning electron microscopy and X-ray microtomography. Immersion in simulated body fluid resulted in rapid formation of carbonated hydroxyapatite, as confirmed by X-ray diffraction, Fourier transform infrared spectroscopy, and energy dispersive spectroscopy, which showed enhanced biological activity. The Ca/P molar ratio was similar to that of natural bone, and flow cytometry confirmed non-cytotoxicity. The combination of 58S and 13-93 bioactive glasses resulted in scaffolds with balanced mechanical and biological properties, providing an efficient and cost-effective approach for tissue engineering applications.

KEYWORDS: Bioactive glasses; 58S; 13-93; Freeze-casting; Mechanical behavior; *In vitro* assays.

1. INTRODUCTION

The class of bioactive glasses includes a wide range of materials that have been used in regenerative medicine, particularly in bone tissue engineering. It dates back to the 1960s and is associated with the pioneering work of Prof. Larry Hench and co-workers [1]. This bioactive glass is called 45S5 and has the following chemical composition: SiO_2 (45 wt.%), Na_2O (24.5 wt.%), CaO (24.5 wt.%), and P_2O_5 (6 wt.%). This historic

achievement marked a breakthrough innovation in biomaterials and led to the commercial production of Bioglass® [2]. This material is recognized for its ability to promote integration with living tissues [3]. While Hench originally produced Bioglass® using a melt-quenching approach, the sol-gel process has gained considerable attention over the past decades [4]. Sol-gel materials can have tailored pore structure, particle size, and surface morphology [5,6]. Such properties can be useful for promoting cell migration, adhesion, proliferation, and differentiation, thus favoring tissue repair [7]. In addition, the sol-gel process offers virtually limitless possibilities for the production of glasses with a wide variety of compositions, driving innovation in the field of regenerative medicine.

58S bioactive glass consists of 58 wt.% SiO_2, 33 wt.% CaO and 9 wt.% P_2O_5. Its high reactivity in aqueous environments, due to its high CaO content and CaO/P_2O_5 ratio, promotes integration into physiological environments and facilitates the formation of strong bonds with bone and cartilage tissues [8]. During the initial post-implantation phase, the high specific surface area of sol-gel-derived 58S promotes surface reactions *in vivo*, leading to rapid ionic dissolution and the formation of a carbonated hydroxyapatite (HAp) layer. This process is critical because it triggers the release of soluble Si species, along with Ca and P ions, which subsequently activate gene expression and promote accelerated bone formation [9,10]. However, 58S glass is reported to have a low crystallization temperature of about 650 °C, probably due to the segregation of calcium phosphate from silica during the dehydration process [11,12]. This segregation and subsequent crystallization can not only hinder the sintering process but also reduce the bioactivity and biodegradability of the glass. In a recent work [13], we prepared freeze-cast 58S scaffolds for bone tissue engineering. Due to the poor

sinterability of 58S, these materials required heat treatment at 1250 °C for 2 h. This elevated temperature caused 58S to crystallize, which negatively affected its biological behavior.

The 13-93 bioactive glass has the following chemical composition: SiO_2 (53 wt.%), CaO (20 wt.%), Na_2O (6 wt.%), P_2O_5 (4 wt.%), K_2O (12 wt.%), and MgO (5 wt.%) [14]. Due to the presence of network modifiers such as K_2O and MgO in its composition, this material has a reduced tendency to crystallize and a lower melting temperature compared to other bioactive glasses. As a result, it has a wide temperature window between the glass transition temperature (T_g) and the crystallization temperature (T_c), facilitating viscous flow sintering and providing superior densification without inducing crystallization [15,16]. Additionally, both CaO and MgO have been shown to contribute to surface reaction kinetics, promoting new bone formation and improving bone cell adhesion and stability [17]. However, 13-93 glass typically has a low specific surface area, which can negatively impact its dissolution rate and biological behavior [18].

In this study, we developed freeze-cast scaffolds by blending 13-93 and 58S bioactive glasses to combine the low crystallization tendency of 13-93 with the high surface area and bioactivity of 58S. In addition, the overall mechanical properties of the composite structures are expected to be improved by the incorporation of 13-93 glass, which is known for its high mechanical strength [17]. The freeze-casting process was chosen to produce the scaffolds because of its flexibility, feasibility, and scalability [19]. As far as we know, this is the first time that the fabrication of freeze-cast 58S/13-93 composite scaffolds has been reported in the literature. This study represents a significant advance

in regenerative medicine by introducing highly porous and mechanically robust scaffolds that can be prepared at a low sintering temperature of 650 °C. This breakthrough offers significant advantages in terms of energy efficiency, cost-effectiveness, and reduced fabrication time, thereby improving the feasibility and scalability of scaffold fabrication for tissue engineering applications.

2. MATERIALS AND METHODS

2.1. STARTING MATERIALS

Tetraethyl orthosilicate (TEOS, Aldrich, 98%), triethyl phosphate (TEP, Aldrich, ≥ 99.8%), and calcium nitrate tetrahydrate ($Ca(NO_3)_2{\cdot}4H_2O$, Aldrich, 99%) were employed in the preparation of 58S glass. Sodium nitrate ($NaNO_3$, Aldrich, 99%), potassium nitrate (KNO_3, Aldrich, ≥ 98%), and magnesium nitrate hexahydrate ($Mg(NO_3)_2{\cdot}6H_2O$, Anidrol, P.A.) were also used in the processing of 13-93 glass. Deionized Milli-Q water (18.2 MΩ at 25 °C) and nitric acid (HNO_3, Anidrol, 65%) were also used in the sol-gel processing of the glass samples. For the freeze-casting step, deionized water, citric acid (CA, Synth, ≥ 99.5%), and polyvinyl alcohol (PVA, M_w = 9,000-10,000 $g.mol^{-1}$, Aldrich, 80% hydrolyzed) were employed as the solvent, dispersing agent, and binder, respectively.

2.2. SOL-GEL PROCESS

The sol-gel routes described by Pereira *et al.* [20] and Deliormanli *et al.* [14] were used as references for the synthesis of 58S and 13-93 bioactive glasses, respectively.

- 58S GLASS

H_2O and HNO_3 were first mixed under stirring at room temperature, keeping the pH of the solution close to 2. TEOS was then added and the mixture was stirred for 1 h. The molar ratio of TEOS: H_2O was fixed at 12: 1. TEP and $Ca(NO_3)_2{\cdot}4H_2O$ were added to the solution, the latter one hour after the former, and the prepared solution was then stirred at room temperature for 1 h. The prepared sol-gel solution was poured into polytetrafluoroethylene (PTFE) molds, sealed, and aged at 60 °C for 72 h. The resulting monoliths were powdered and air dried at a maximum temperature of 120 °C for up to 5 days, increasing the temperature by 10 °C each day until 120 °C was reached. The resulting powder was then thermally treated in air at 650 °C for 2 h at a heating rate of 1 $°C.min^{-1}$. Finally, the prepared materials were dry ball milled for 12 h.

- 13-93 GLASS

An aqueous solution of 0.3M HNO_3 was initially prepared at room temperature. TEOS was then added and the system was stirred at room temperature until homogenized, while maintaining the H_2O: TEOS molar ratio at 15: 1. TEP, $NaNO_3$, $Ca(NO_3)_2{\cdot}4H_2O$, KNO_3, and $Mg(NO_3)_2{\cdot}6H_2O$ were then added sequentially. Each precursor was added approximately 30 min after the previous one to ensure homogeneity. After adding KNO_3, the system was heated to 60 °C to promote its complete dissolution. The prepared solution was stirred in a closed flask for 2 h and then allowed to stand at room temperature for 3 days to allow gel formation. The flask was then partially opened and the gel was aged at 60 °C for 48 h before air drying at 120 °C for 24 h. The dried

sample was then heat-treated in air at 625 °C for 4 h at a heating rate of 1 °C.min^{-1}. Finally, it was then dry ball milled for 12 h.

2.3. FREEZE-CASTING

58S and 13-93 glass particles were dispersed in H_2O with the addition of 1 wt% CA as a dispersing agent, followed by stirring for 1 h at room temperature. The mass ratio of 58S to 13-93 was varied to 30:70, 50:50, or 70:30 while maintaining a constant solid loading of 20 vol%. Then, 2 wt% PVA was added and stirred for another hour to allow the polymer to act as a binder and ensure the structural integrity of the green bodies in subsequent steps. The suspension was sonicated for 10 min to remove air bubbles and disperse particle clusters before being poured into cylindrical PTFE molds 10 mm in diameter and 30 mm in height. Freezing was performed with a copper cold finger in a refrigerator maintained at approximately -19°C, using a unidirectional process from bottom to top. The resulting green bodies were freeze-dried and subsequently sintered in air at a heating rate of 1 °C.min^{-1}. The heat treatment program consisted of a 30 min hold at 100 °C followed by a 2 h hold at 300 °C and a final 2 h hold at 650 °C. A schematic of the processing route used in this study is shown in Fig. 1.

2.4. STRUCTURAL CHARACTERIZATION

X-ray powder diffraction (XRD) was performed using a Philips-PANalytical PW 1710 diffractometer operating at 40 kV and 30 mA, with a step size of 0.06° and using CuKα radiation. Laser granulometry was performed with a Cilas 1064 apparatus using water as the dispersion medium. Fourier transform infrared spectroscopy (FTIR) was performed on a Bruker Alpha spectrometer with a resolution of 4 cm^{-1} and 128 scans.

An attenuated total reflectance (ATR) accessory and a diamond crystal were used in these analyses. N_2 adsorption was carried out in a Quantachrome Nova 1200e system using samples outgassed under vacuum at 150 °C for 12 h. Scanning electron microscopy (SEM) analysis was performed using Jeol JSM-6360LV and FEI Quanta 200 microscopes at an accelerating voltage of 10 kV. Powder samples were dispersed in acetone and sonicated for 5 min at room temperature prior to deposition on silicon substrates. Scaffold samples were attached to stubs using double-sided carbon tape. Before SEM analysis, the samples were sputter coated with a 10 nm thick gold film. Energy dispersive spectroscopy (EDS) analysis was performed using NORAN systems coupled to the electron microscopes. X-ray microtomography (micro-CT) was conducted on a Bruker SkyScan 1174 system using an X-ray voltage of 50 kV, 800 μA, with a voxel size of about 14 μm and 3D thresholding (Otsu Method). The measurements of the porosity (open, closed, and total) were carried out according to the Archimedes method using a Marte AD330 balance. Samples were first weighed dry, then immersed in water, and subjected to a vacuum of 160 mm Hg for 10 min to ensure complete pore saturation. The wet mass of the immersed samples was then recorded. Open and closed porosity fractions were calculated using density values obtained from He pycnometry (2.70 $g.cm^{-3}$ for 58S glass and 2.65 $g.cm^{-3}$ for 13-93 glass) and the corresponding equations [21]. Compression tests were performed at room temperature using a Shimadzu AGS-X universal testing machine with a crosshead displacement speed of 0.01 $mm.s^{-1}$ and a 5 kN load cell.

2.6. *IN VITRO* ASSAYS

- BIOACTIVITY

Soaking biomaterials in simulated body fluid (SBF) is a standardized approach to evaluate the bioactivity of a biomaterial, making it particularly relevant for bone tissue engineering applications [22,23]. In this study, following the method described by Kokubo and Takadama [24], the SBF solution was prepared and the samples were soaked in SBF at a concentration of 1.5 $g.L^{-1}$ at 37 °C for up to 14 days. The samples were then thoroughly washed with water and air dried at 40 °C for 24 h for examination by SEM, EDS, FTIR, and XRD.

- BIOCOMPATIBILITY

The MRC5 cell line, derived from normal human fetal lung tissue, was used to evaluate the biocompatibility of the prepared samples by flow cytometry. Cells were cultured in Dulbecco's modified Eagle's medium (DMEM, Sigma-Aldrich) supplemented with 10% fetal bovine serum and 2% antifungal antibiotic solution (PSA: penicillin, streptomycin, and amphotericin, Sigma-Aldrich) under controlled conditions (5% CO_2, 37 ºC, and high humidity). After reaching the appropriate confluence, approximately 1.0×10^8 cells were transferred to 12-well plates and allowed to adhere for 24 h. Cytotoxicity evaluation was performed according to ISO 10993-12 (*Biological evaluation of medical devices – Part 12: Sample preparation and reference materials*) using the extract method. The scaffolds were sterilized under ultraviolet (UV) light for 4 h and then incubated in DMEM (10 $g.L^{-1}$) for 24 ± 2 h at 37 ± 1 ºC to obtain a liquid extract. The extract obtained was applied directly to the cells, replacing the medium without filtering. The experimental groups (n = 3 per group) included: (i) sterile NaCl solution (0.9% w/v) as a negative control, (ii) 20% DMSO solution as a positive control, and (iii)

the liquid extract from the scaffolds. Flow cytometry was performed using the Fixable Viability Stain® V450 reagent, which differentiates viable cells from non-viable cells. This reagent exhibits maximum fluorochrome emission at 450 nm and covalently binds to cell surface and intracellular amines. As a result, non-viable cells show increased fluorescence compared to viable cells. A total of 50,000 events were collected per sample. Cells and controls were visually inspected for cytotoxicity-related morphologic changes, including early/late apoptosis, necrosis, cell condensation, apoptotic blebs, and cytoskeletal disruptions. Imaging was conducted in bright field mode at 20-40× magnification using a dye.

3. RESULTS AND DISCUSSION

3.1. BIOACTIVE GLASSES

The XRD patterns obtained for 13-93 and 58S glasses are shown in Fig. 2a. Both materials have a broad halo centered at about 2θ = 28°, which is characteristic of amorphous materials [25]. The XRD pattern of the 58S glass shows diffraction peaks at 2θ = 32° and 42°, which can be attributed to the presence of small amounts of wollastonite ($CaSiO_3$) or β-tricalcium phosphate (β-TCP) within the glass network [26]. For 13-93 glass, incomplete dissolution or subsequent formation of nitrate crystals, such as sodium nitrate, may have occurred. Specifically, the diffraction peak at 2θ = 30° corresponds to $NaNO_3$, while the peak at 35° indicates the presence of both $NaNO_3$ and β-tricalcium phosphate (β-TCP). In addition, β-TCP is observed in the peak at 2θ = 45° [15].

Fig. 2b exhibits the N_2 adsorption isotherms taken for these glasses. Both samples exhibit a hysteresis loop indicating that capillary condensation of N_2 occurs within the mesopores. However, this loop is more pronounced in 58S compared to 13-93, indicating a larger volume of mesopores (pore sizes ranging from 2 nm to 50 nm) in the former. This finding is consistent with the significantly higher gas adsorption observed for 58S (about 300 $cm^3.g^{-1}$) compared to 13-93 (about 2.5 $cm^3.g^{-1}$). The specific surface area, evaluated by the Brunauer-Emmett-Teller (BET) method, was found to be 280 $m^2.g^{-1}$ for 58S and 2 $m^2.g^{-1}$ for 13-93. This result is in line with the literature, as 13-93 glass has been reported to have a low specific surface area [18]. In contrast, sol-gel-derived 58S glass is known for its mesoporous structure and high surface area [27]. These properties are the basis for its potential use in regenerative medicine.

Fig. 2c shows the FTIR spectra obtained for these glasses. The absorption bands at 1030 cm^{-1} and 1330 cm^{-1} are assigned to the asymmetric stretching of Si-O-Si bonds, while the band at 450 cm^{-1} corresponds to the bending mode of these bonds [28–31]. The bands at 960 cm^{-1} and 1630 cm^{-1} are related to silanol (Si-OH) groups [32] and physisorbed water [33], respectively. The band at 1425 cm^{-1} has been related to CO_3^{2-} groups [34]. The band at 820 cm^{-1} corresponds to the vibrational modes of Si-O-2NBO (non-bridging oxygen) bonds associated with the presence of network modifiers in the glass composition. The incorporation of alkali (Na^+, K^+) and alkaline earth (Ca^{2+}, Mg^{2+}) ions into 13-93 bioactive glass weakens the Si-O network by forming NBOs. A lower melting temperature results from this disruption of the glass structure [35,36]. Hydroxyl groups are responsible for the broad absorption band centered at about 3400 cm^{-1} [33]. Fig. 2d exhibits SEM micrographs taken for 13-93 and 58S glasses. These images show that 13-93 glass has a finer particle size distribution than 58S, as confirmed by laser

granulometry (mean particle size of 7 μm for 13-93 and 18 μm for 58S). In addition, the SEM images show particles with irregular shapes and varying sizes, behavior typically observed in mechanically comminuted materials. This is consistent with the 12 h ball milling process used after the sol-gel process. As previously reported [27], 58S particles have a porous texture while 13-93 particles have a denser structure. This textural difference probably contributes to the larger specific surface area observed for 58S compared to 13-93 (280 $m^2.g^{-1}$ *vs.* 2 $m^2.g^{-1}$).

3.2 FREEZE-CAST SCAFFOLDS

- STRUCTURAL AND MECHANICAL PROPERTIES

Fig. 3 shows SEM micrographs of a freeze-cast scaffold (a) before and (b) after heat treatment. As shown in Fig. 3a, the controlled unidirectional freezing process results in aligned pores extending from bottom to top. This lamellar pore architecture results from the use of water in the initial suspensions, as ice crystals are reported to solidify in such a morphology [37,38]. However, upon heat treatment, the pore shape changes to a spherical configuration (Fig. 3b). This change is likely due to the softening of the glass mixture at the sintering temperature, which is close to the reported T_g of 660 °C for 13-93 glass [18]. This behavior is an indication that the material undergoes viscous flow during heat treatment, resulting in the change in pore structure observed in Fig. 3b. In contrast, 58S has a higher T_g of approximately 785 °C [39]. This result highlights the critical importance of understanding the thermal dynamics of bioactive glass scaffolds to optimize processing parameters and achieve the desired structures for bone tissue engineering applications.

Fig. 4a depicts the shrinkage of the prepared scaffolds after the sintering process. While no significant difference in shrinkage was observed with increasing the 58S/13-93 mass ratio from 30/70 to 50/50 (24.3 ± 2.3% *vs.* 23.7 ± 1.7%), a significant reduction in shrinkage occurred at the 70/30 ratio (13.6 ± 1.1%). Thus, it was found that the higher the loading of 58S in the prepared scaffolds, the less the shrinkage during sintering. This finding underscores the complex interplay of starting material properties in scaffold fabrication and highlights the significant effect of adjusting the 58S/13-93 mass ratio on scaffold shrinkage during the sintering process. This behavior can be attributed to the softening of 13-93 glass. As mentioned above, this bioactive glass is reported to have a T_g of about 660 °C [18], indicating its susceptibility to softening when heated to 650 °C for 2 h. Conversely, the 58S bioactive glass has a higher T_g of up to 785 °C [39], an indication that its softening during sintering is less pronounced. Fig. 4b shows the evaluation of open, closed, and total porosity for these materials as measured by Archimedes tests. The reduction in shrinkage observed for the 70/30 sample coincided with a significant increase in total porosity, which was measured to be 76.3 ± 2.6%. In comparison, the total porosity evaluated for the 30/70 and 50/50 samples was 70.1 ± 2.4% and 73.3 ± 4.9%, respectively. It is also noteworthy that the presence of closed pores in the prepared specimens is low (less than 7%), a behavior that has previously been observed in freeze-cast specimens [13,18]. Open pores offer distinct advantages for scaffolds, facilitating integration with the physiological environment and allowing migration of cells and capillaries. This property is critical for tissue engineering applications where seamless interaction between the scaffold and the surrounding tissue is essential for successful regeneration. Fig. 4c shows typical micro-CT images obtained for a sintered scaffold, revealing the presence of lamellar pores arranged in an ordered

fashion. This organized pore structure holds promise for optimizing scaffold architecture to mimic the complexity of native tissue, thereby enhancing biocompatibility and therapeutic efficacy. Notably, as recommended for effective bone grafting applications, all scaffolds have mean pore sizes in the range of 95-105 μm [40]. This pore size range allows for proper cell infiltration and nutrient diffusion, which are critical for successful tissue regeneration [41]. The comprehensive analysis of scaffold properties shown in Fig. 4 highlights the intricate relationship between material composition, shrinkage behavior, and the resulting pore structure.

Fig. 5a shows the compressive strength of the composite scaffolds fabricated in this study. The data show significant variations in compressive strength for different 58S/13-93 mass ratios. Specifically, the compressive strengths were 11.25 ± 2.48 MPa, 4.65 ± 0.45 MPa, and 3.84 ± 1.77 MPa for the 30/70, 50/50, and 70/30 ratios, respectively. The corresponding Young's modulus values were 0.81 ± 0.27 GPa, 0.43 ± 0.08 GPa, and 0.26 ± 0.14 GPa for the same ratios. These results reveal a clear correlation between the amounts of 58S and 13-93 in the composite samples. Specifically, lower concentrations of 58S and higher amounts of 13-93 are associated with increased compressive strength in the resulting scaffolds. This result is likely due to the viscous flow of 13-93 glass during sintering, which reduces the porosity (Fig. 4b) and increases the mechanical strength (Fig. 5a) of the composite scaffolds. For reference, pure 58S freeze-cast scaffolds with approximately 64% porosity, sintered at 1250 ºC for 2 h, exhibited a compressive strength of 1.52 ± 0.30 MPa [13]. In addition, pure 13-93 glass scaffolds with similar porosity heat treated at 650 ºC for 2 h showed a compressive strength of 22.4 ± 3.1 MPa [18].

Fig. 5b to Fig. 5d show SEM micrographs of the prepared materials, in particular, the densification of the pore structure in the 30/70 samples and round pores with a size of about 60 μm, indicating the occurrence of viscous flow during the sintering process. Samples prepared with this mass ratio have a total porosity of 70.1 ± 2.4% (Fig. 4b), the lowest of the samples due to the viscous flow influence and the highest compressive strength of 11.25 ± 2.48 MPa (Fig. 5a), and Young's modulus of 0.81 ± 0.27 GPa. These properties make this material a promising candidate for bone tissue engineering applications, especially for low-loading situations that resemble trabecular bone. For comparison, Young's modulus of human trabecular bone from the distal femur is in the range of 0.01-3 GPa, with different values of compressive strength depending on bone age and experimental condition, but usually in the range of 2-12 MPa [40,42–44]. The mechanical properties of the 30/70 composite scaffold are similar to those of trabecular bone, enhancing its potential use in regenerative medicine. This increases the longevity of the implant, potentially eliminating the need for further surgery for removal or replacement, thereby improving the patient's quality of life.

- BIOACTIVITY

Fig. 6a and Fig. 6b show the XRD pattern and FTIR spectra of scaffolds soaked in SBF for up to 14 days. The diffraction peaks highlighted in Fig. 6a correspond to HAp as identified by reference to JCPDS Card File No. 09-0432. The absorption bands shown in Fig. 6b also indicate the presence of HAp. In particular, the bands at 1020 cm^{-1}, 600 cm^{-1}, and 560 cm^{-1} are attributed to PO_4^{3-} groups from HAp [45]. The SEM micrographs in Fig. 7a, Fig. 7b, and Fig. 7c illustrate scaffolds prepared with mass ratios of 58S/13-93 of 30/70, 50/50, and 70/30, respectively. These images show

nodules characteristic of HAp crystals in all samples. Fig. 7d shows that EDS analysis confirms the presence of HAp with a Ca/P ratio of 1.38, which is important for evaluating scaffold bioactivity. Ideally, HAp is associated with a Ca/P ratio of 1.67, which closely resembles the mineral phase of human bone and is therefore well suited for the formation of bioactive layers.

The appearance of HAp crystals is significantly enhanced with increasing amounts of 58S in the samples. For instance, the scaffolds revealed the formation of HAp within the first day of soaking in SBF, faster than pure 13-93 scaffolds reported elsewhere [18]. This trend can be attributed to the significantly higher specific surface area of 58S compared to 13-93, which was measured to be approximately 280 $m^2.g^{-1}$ and 2 $m^2.g^{-1}$, respectively (Fig. 2). The increased surface area of 58S allows for greater interaction with the physiological environment, thereby accelerating HAp formation.

- BIOCOMPATIBILITY

In this study, the biocompatibility of the prepared freeze-cast scaffolds was evaluated by flow cytometry. The proportions of live and dead cells were determined, along with control groups, and the results are summarized in Table 1. The data indicated that the scaffolds exhibited low cytotoxicity, with relative cell viability greater than 80% in all sample extracts tested. Fig. 8 provides detailed dot plot panels for (a) the negative control group and (b) cells treated with the composite scaffold extract. Specifically, Fig. 8a, showing the SSC *vs.* FSC panel, shows a well-defined population of healthy cells and normal cell debris, with high values for both parameters. Conversely, the SSC *vs.* 7-AAD panel allows the identification of two distinct cell populations based on

7-AAD staining: live cells (low levels of 7-AAD) and dead cells. Fig. 8b shows data for cells treated with the 30/70 composite scaffold extract. The SSC *vs.* FSC scatter plot in this figure shows a pattern similar to that observed in the negative control sample (Fig. 8a), confirming the biocompatible behavior of the tested sample. In addition, the SSC *vs.* 7-AAD scatter plot in Fig. 8b also supports the biocompatibility profile, showing a small population of dead cells similar to the negative control. FSC indicates cell size, while SSC indicates internal complexity or cell granularity. The 7-AAD axis represents the fluorescence intensity of this dye, which binds to the DNA of dead cells. Cells with high fluorescence on the x-axis are considered dead because 7-AAD can only infiltrate cells with compromised membranes. There is no universal cut-off point for SSC-A to define live or dead cells, as this can vary depending on the cell type and specific experiment. However, SSC-A helps distinguish between different cell types and their internal complexity. In the plot provided, granularity appears to be less critical for distinguishing between live and dead cells, as both types are distributed throughout the SSC-A range.

The morphological characterization of cells is available in Fig. 9. The images exhibit confluent cultures characterized by high cell density and uniformly shaped, well-spread cultures, indicating healthy growth and viability. These observations are in accordance with flow cytometry data. Furthermore, the spindle-shaped, elongated morphology of treated cells also indicates active cell proliferation, and no significant signs of cytotoxicity such as cell rounding, detachment, or debris were observed, indicating that the materials tested did not induce significant cytotoxic effects under the conditions used [46]. The high confluence without significant cell detachment suggests that the cells are well-adherent and experiencing minimal cytotoxic stress.

4. CONCLUSIONS

The primary objective of this study was to fabricate scaffolds using 58S and 13-93 bioactive glasses by freeze-casting particulate slurries and to investigate the effects of different glass ratios on the resulting properties. Sintering at 650 °C effectively removed organic compounds while preserving the amorphous structure of both glasses, as confirmed by post-sintering XRD patterns showing little evidence of crystallization. Porosity assessments using Archimedes' principle, SEM examination, and micro-CT analysis consistently indicated that the scaffold's porosity was above 70%, with a high degree of interconnected pores, suitable for regenerative medicine applications. In particular, the scaffold with a 58S/13-93 mass ratio of 30/70 had the lowest porosity (70.1 ± 2.4%), along with increased compressive strength (11.25 ± 2.48 MPa) and Young's modulus (0.81 ± 0.27 GPa). In addition, this scaffold showed no cytotoxic behavior in flow cytometry assays and demonstrated enhanced biological activity as evidenced by the rapid formation of HAp crystals after immersion in SBF. While scaffolds with higher 58S content exhibited greater bioactivity, flow cytometry panels confirmed that scaffold extracts are a reliable method for assessing low cytotoxicity; however, direct contact assays could provide more detailed interactions between NRC-5 cells and the bioactive glasses. This study demonstrates the efficacy of combining 58S and 13-93 bioactive glasses to create amorphous bioactive scaffolds with well-balanced physical properties and biological responses, even at relatively low sintering temperatures of 650 °C. Such an approach offers significant advantages in terms of energy efficiency, reduced processing time, and overall cost-effectiveness.

ACKNOWLEDGEMENTS

The authors thank the financial support of CAPES (PROEX and CAPES PrInt), CNPq (403191/2021-1 and 304415/2021-9), FAPEMIG (APQ-01286-24), and PRPq-UFMG (PROBIC). We also thank the technical assistance of Samuel Lima, Fernando Luciano Souza, Prof. Vicente Buono, Patrícia Azevedo, Prof. Dagoberto Santos, and Leonardo Mayer.

REFERENCES

[1] M. Montazerian, E.D. Zanotto, A guided walk through Larry Hench's monumental discoveries, J. Mater. Sci. 52 (2017) 8695–8732. https://doi.org/10.1007/s10853-017-0804-4.

[2] J.R. Jones, Review of bioactive glass: From Hench to hybrids, Acta Biomater. 9 (2013) 4457–4486. https://doi.org/10.1016/j.actbio.2012.08.023.

[3] L.L. Hench, Bioceramics: From concept to clinic, J. Am. Ceram. Soc. 74 (1991) 1487–1510. https://doi.org/10.1111/J.1151-2916.1991.TB07132.X.

[4] A. Lucas-Girot, F.Z. Mezahi, M. Mami, H. Oudadesse, A. Harabi, M. Le Floch, Sol-gel synthesis of a new composition of bioactive glass in the quaternary system SiO_2-CaO-Na_2O-P_2O_5: Comparison with melting method, J. Non. Cryst. Solids. 357 (2011) 3322–3327. https://doi.org/10.1016/j.jnoncrysol.2011.06.002.

[5] R. Omidi, P. Alizadeh, M. Soltani, Poly (amido amine) G5 modified mesoporous silica-based pH-responsive drug-delivery system for tetracycline and ibuprofen, Int. J. Polym. Mater. Polym. Biomater. 72 (2022) 984–994.

https://doi.org/10.1080/00914037.2022.2071270.

[6] F. Benedetti, L. Amidani, J.S. Pelli Cresi, F. Boscherini, S. Valeri, S. D'Addato, V. Nicolini, G. Malavasi, P. Luches, Role of cerium oxide in bioactive glasses during catalytic dissociation of hydrogen peroxide, Phys. Chem. Chem. Phys. 20 (2018) 23507–23514. https://doi.org/10.1039/c8cp02271b.

[7] B. Zheng, X. Lin, X. Zhang, D. Wu, K. Matyjaszewski, Emerging functional porous polymeric and carbonaceous materials for environmental treatment and energy storage, Adv. Funct. Mater. 30 (2020) 1907006. https://doi.org/10.1002/adfm.201907006.

[8] L. Ji, W. Qiao, K. Huang, Y. Zhang, H. Wu, S. Miao, H. Liu, Y. Dong, A. Zhu, D. Qiu, Synthesis of nanosized 58S bioactive glass particles by a three-dimensional ordered macroporous carbon template, Mater. Sci. Eng. C. 75 (2017) 590–595. https://doi.org/10.1016/j.msec.2017.02.107.

[9] A.B. Houreh, S. Labbaf, H.K. Ting, F. Ejeian, J.R. Jones, M.H.N. Esfahani, Influence of calcium and phosphorus release from bioactive glasses on viability and differentiation of dental pulp stem cells, J. Mater. Sci. 52 (2017) 8928–8941. https://doi.org/10.1007/s10853-017-0946-4.

[10] I.D. Xynos, M.V.J. Hukkanen, J.J. Batten, L.D. Buttery, L.L. Hench, J.M. Polak, Bioglass®45S5 stimulates osteoblast turnover and enhances bone formation in vitro: implications and applications for bone tissue engineering, Calcif. Tissue Int. 67 (2000) 321–329. https://doi.org/10.1007/s002230001134.

[11] J.H. Lopes, O.M.V.M. Bueno, I.O. Mazali, C.A. Bertran, Investigation of citric acid-assisted sol-gel synthesis coupled to the self-propagating combustion method for preparing bioactive glass with high structural homogeneity, Mater.

Sci. Eng. C. 97 (2019) 669–678. https://doi.org/10.1016/j.msec.2018.12.022.

[12] N. Ghaebi Panah, R. Atkin, T.B. Sercombe, Effect of low temperature crystallization on 58S bioactive glass sintering and compressive strength, Ceram. Int. 47 (2021) 30349–30357. https://doi.org/10.1016/j.ceramint.2021.07.215.

[13] D.M.M. dos Santos, S.M. de Carvalho, M.M. Pereira, M. Houmard, E.H.M. Nunes, Freeze-cast composite scaffolds prepared from sol-gel derived 58S bioactive glass and polycaprolactone, Ceram. Int. 45 (2019) 9891–9900. https://doi.org/10.1016/j.ceramint.2019.02.030.

[14] A.M. Deliormanlı, M. Yıldırım, Sol-gel synthesis of 13-93 bioactive glass powders containing therapeutic agents, J. Aust. Ceram. Soc. 52 (2016) 9–19. https://austceram.com/wp-content/uploads/2016/06/2-JACS-52-2-Aylin-9-19.pdf

[15] Q. Nawaz, A. de Pablos-Martín, J. Martins de Souza e Silva, L. Berthold, K. Hurle, A.T. Contreras Jaimes, M. Sitarz, D.S. Brauer, A.R. Boccaccini, Crystallization study of sol-gel derived 13-93 bioactive glass powder, J. Eur. Ceram. Soc. 41 (2021) 1695–1706. https://doi.org/10.1016/j.jeurceramsoc.2020.09.052.

[16] X. Liu, M.N. Rahaman, Q. Fu, A.P. Tomsia, Porous and strong bioactive glass (13-93) scaffolds prepared by unidirectional freezing of camphene-based suspensions, Acta Biomater. 8 (2012) 415–423. https://doi.org/10.1016/j.actbio.2011.07.034.

[17] E. Fiume, C. Migneco, E. Verné, F. Baino, Comparison between bioactive sol-gel and melt-derived glasses/glass-ceramics based on the multicomponent SiO_2-P_2O_5-CaO-MgO-Na_2O-K_2O system, Materials (Basel). 13 (2020) 540. https://doi.org/10.3390/ma13030540.

[18] F.B. Fantecelle, D.M.M. dos Santos, B.R. Barrioni, M.M. Pereira, H.A. Alcamand, M.L. Lapér, M. Houmard, E.H.M. Nunes, Structural, mechanical, and in vitro characterization of freeze-cast scaffolds prepared using a sol-gel-derived bioactive glass from the SiO_2-CaO-Na_2O-P_2O_5-K_2O-MgO system, Ceram. Int. 49 (2023) 2183–2193. https://doi.org/10.1016/j.ceramint.2022.09.185.

[19] M.-A. Shahbazi, M. Ghalkhani, H. Maleki, Directional freeze-casting: A bioinspired method to assemble multifunctional aligned porous structures for advanced applications, Adv. Eng. Mater. 22 (2020) 2000033. https://doi.org/10.1002/adem.202000033.

[20] M.M. Pereira, A.E. Clark, L.L. Hench, Calcium phosphate formation on sol-gel-derived bioactive glasses in vitro, J. Biomed. Mater. Res. 28 (1994) 693–698. https://doi.org/10.1002/jbm.820280606.

[21] A. Coulon, M. Cohen, G. Pillet, Light-weighing traditional ceramics by porosity control and consequences on mechanical strength, Ceram. Int. 50 (2024) 6001–6008. https://doi.org/10.1016/j.ceramint.2023.11.269.

[22] J. Faure, R. Drevet, A. Lemelle, N. Ben Jaber, A. Tara, H. El Btaouri, H. Benhayoune, A new sol-gel synthesis of 45S5 bioactive glass using an organic acid as catalyst, Mater. Sci. Eng. C. 47 (2015) 407–412. https://doi.org/10.1016/j.msec.2014.11.045.

[23] L.M. Henning, S. Zavareh, P.H. Kamm, M. Höner, H. Fischer, J. Banhart, F. Schmidt, A. Gurlo, Manufacturing and characterization of highly porous bioactive glass composite scaffolds using unidirectional freeze casting, Adv. Eng. Mater. 19 (2017) 1–9. https://doi.org/10.1002/adem.201700129.

[24] T. Kokubo, H. Takadama, How useful is SBF in predicting in vivo bone

bioactivity?, Biomaterials. 27 (2006) 2907–2915. https://doi.org/10.1016/j.biomaterials.2006.01.017.

[25] Q. Nawaz, M.A.U. Rehman, A. Burkovski, J. Schmidt, A.M. Beltrán, A. Shahid, N.K. Alber, W. Peukert, A.R. Boccaccini, Synthesis and characterization of manganese containing mesoporous bioactive glass nanoparticles for biomedical applications, J. Mater. Sci. Mater. Med. 29 (2018) 667–674. https://doi.org/10.1007/s10856-018-6070-4.

[26] A. Balamurugan, G. Sockalingum, J. Michel, J. Fauré, V. Banchet, L. Wortham, S. Bouthors, D. Laurent-Maquin, G. Balossier, Synthesis and characterisation of sol gel derived bioactive glass for biomedical applications, Mater. Lett. 60 (2006) 3752–3757. https://doi.org/10.1016/j.matlet.2006.03.102.

[27] P. Sepulveda, J.R. Jones, L.L. Hench, Characterization of melt-derived 45S5 and sol-gel-derived 58S bioactive glasses, J. Biomed. Mater. Res. 58 (2001) 734–740. https://doi.org/10.1002/jbm.10026.

[28] J. Serra, P. González, S. Liste, C. Serra, S. Chiussi, B. León, M. Pérez-Amor, H.O. Ylänen, M. Hupa, FTIR and XPS studies of bioactive silica based glasses, J. Non. Cryst. Solids. 332 (2003) 20–27. https://doi.org/10.1016/j.jnoncrysol.2003.09.013.

[29] G. Luo, Y. Ma, X. Cui, L. Jiang, M. Wu, Y. Hu, Y. Luo, H. Pan, C. Ruan, 13-93 bioactive glass/alginate composite scaffolds 3D printed under mild conditions for bone regeneration, RSC Adv. 7 (2017) 11880–11889. https://doi.org/10.1039/c6ra27669e.

[30] A.M. Deliormanli, Preparation, in vitro mineralization and osteoblast cell response of electrospun 13-93 bioactive glass nanofibers, Mater. Sci. Eng. C. 53

(2015) 262–271. https://doi.org/10.1016/j.msec.2015.04.037.

[31] Q. Fu, M.N. Rahaman, B.S. Bal, W. Huang, D.E. Day, Preparation and bioactive characteristics of a porous 13-93 glass, and fabrication into the articulating surface of a proximal tibia, J. Biomed. Mater. Res. Part A. 82A (2007) 222–229. https://doi.org/10.1002/jbm.a.31156.

[32] H. Yoshino, K. Kamiya, H. Nasu, IR study on the structural evolution of sol-gel derived SiO_2 gels in the early stage of conversion to glasses, J. Non. Cryst. Solids. 126 (1990) 68–78. https://doi.org/10.1016/0022-3093(90)91024-L.

[33] R.M. Almeida, C.G. Pantano, Structural investigation of silica gel films by infrared spectroscopy, J. Appl. Phys. 68 (1990) 4225–4232. https://doi.org/10.1063/1.346213.

[34] M. Raz, F. Moztarzadeh, S.S. Kordestani, Sol-gel based fabrication and properties of Mg-Zn doped bioactive glass/gelatin composite scaffold for bone tissue engineering, Silicon. 10 (2018) 667–674. https://doi.org/10.1007/s12633-016-9510-0.

[35] C.B. Carter, M.G. Norton, Complex crystal and glass structures, in: C.B. Carter, M.G. Norton (Eds.), Ceram. Mater. Sci. Eng., Springer New York, New York, NY, 2007: pp. 100–119. https://doi.org/10.1007/978-0-387-46271-4_7.

[36] A.J. Salinas, S. Shruti, G. Malavasi, L. Menabue, M. Vallet-Regí, Substitutions of cerium, gallium and zinc in ordered mesoporous bioactive glasses, Acta Biomater. 7 (2011) 3452–3458. https://doi.org/10.1016/j.actbio.2011.05.033.

[37] W.L. Li, K. Lu, J.Y. Walz, Freeze casting of porous materials: review of critical factors in microstructure evolution, Int. Mater. Rev. 57 (2012) 37–60.

https://doi.org/10.1179/1743280411Y.0000000011.

[38] T. Waschkies, R. Oberacker, M.J. Hoffmann, Control of lamellae spacing during freeze casting of ceramics using double-side cooling as a novel processing route, J. Am. Ceram. Soc. 92 (2009) S79–S84. https://doi.org/10.1111/j.1551-2916.2008.02673.x.

[39] K. Huang, S. Cai, G. Xu, M. Ren, X. Wang, R. Zhang, S. Niu, H. Zhao, Sol-gel derived mesoporous 58S bioactive glass coatings on AZ31 magnesium alloy and in vitro degradation behavior, Surf. Coatings Technol. 240 (2014) 137–144. https://doi.org/10.1016/j.surfcoat.2013.12.026.

[40] Y. Liu, J.K.Y. Chan, S.-H. Teoh, Review of vascularised bone tissue-engineering strategies with a focus on co-culture systems, J. Tissue Eng. Regen. Med. 9 (2015) 85–105. https://doi.org/10.1002/term.1617.

[41] J. Li, X. Yuan, F. He, A.F.T. Mak, Hybrid coating of hydroxyapatite and collagen within poly(D,L-lactic-co-glycolic acid) scaffold, J. Biomed. Mater. Res. Part B Appl. Biomater. 86B (2008) 381–388. https://doi.org/10.1002/jbm.b.31031.

[42] T.C. Yang Harmony, N. Yusof, S. Ramalingam, R. Baharin, A. Syahrom, A. Mansor, Deep-freezing temperatures during irradiation preserves the compressive strength of human cortical bone allografts: A cadaver study, Clin. Orthop. Relat. Res. 480 (2022) 407–418. https://doi.org/10.1097/CORR.0000000000001968.

[43] F. Li, J. Li, G. Xu, G. Liu, H. Kou, L. Zhou, Fabrication, pore structure and compressive behavior of anisotropic porous titanium for human trabecular bone implant applications, J. Mech. Behav. Biomed. Mater. 46 (2015) 104–114. https://doi.org/10.1016/j.jmbbm.2015.02.023.

[44] A. Mansoori-Kermani, S. Mashayekhan, F. Kermani, M.J. Abdekhodaie, The effect of tricalcium silicate incorporation on bioactivity, injectability, and mechanical properties of calcium sulfate/bioactive glass bone cement, Ceram. Int. 49 (2023) 15003–15014. https://doi.org/10.1016/j.ceramint.2023.01.083.

[45] H. Gheisari, E. Karamian, M. Abdellahi, A novel hydroxyapatite - Hardystonite nanocomposite ceramic, Ceram. Int. 41 (2015) 5967–5975. https://doi.org/10.1016/j.ceramint.2015.01.033.

[46] H.S. Budi, M.C. Setyawati, S. Anitasari, Y.-K. Shen, I. Pebriani, D.E. Ramadan, Cell detachment rates and confluence of fibroblast and osteoblast cell culture using different washing solutions, Brazilian J. Biol. 84 (2024) e265825. https://doi.org/10.1590/1519-6984.265825.

FIGURE CAPTIONS

- Figure 1: Schematic of the processing route used in this study.

- Figure 2: (a) XRD patterns, (b) N_2 sorption isotherms, (c) FTIR spectra, and (d) SEM micrographs obtained for 13-93 and 58S glasses. In Figure (b), closed and open symbols represent the adsorption and desorption branches, respectively.

- Figure 3: SEM micrographs of freeze-cast scaffolds (a) before and (b) after the heat treatment step. Arrows indicate the direction of the pores before heat treatment. Images obtained for scaffolds prepared using a 70/30 mass ratio of 58S/13-93.

- Figure 4: (a) Volumetric Shrinkage observed during sintering, (b) porosity measured by Archimedes tests, (c) micro-CT images showing the typical morphology of a sintered 70/30 scaffold, and (d) pore size distributions determined by micro-CT analysis with an image pixel size of approximately 15 μm.

- Figure 5: (a) Compressive strength and Young's modulus, (b-d) SEM micrographs of freeze-cast scaffolds prepared with different mass ratios of 58S to 13-93.

- Figure 6: (a) XRD patterns and (b) FTIR spectra taken for samples soaked in SBF for up to 14 days.

- Figure 7: (a-c) SEM micrographs and (d) typical EDS spectrum obtained for scaffolds immersed in SBF for different times. For the samples shown in (a), (b), and (c), the 58S/13-93 mass ratios used were 30/70, 50/50, and 70/30, respectively.

- Figure 8: Representative flow cytometry panels obtained in this study for (a) control groups and (b) composite scaffold 30/70.

- Figure 9: Photomicrograph of NRC-5 cells cultured on composite scaffolds prepared in this work. *Fusiform healthy cell; **Rounded cell attached to the substrate; ***Detached rounded cell.

HIGHLIGHTS

- Scaffolds prepared from 58S and 13-93 bioactive glasses using freeze-casting.
- 30/70 mass ratio of 58S/13-93 yielded scaffolds with optimal properties.
- Samples with high porosity (over 70%) and compressive strength (above 11 MPa).
- Sintering at 650 °C for 2 hours preserved amorphous structure and bioactivity.
- Energy-efficient approach reduces processing time and overall costs.

Table 1: Average percentage of live, dead, and viable cells for each of the prepared composite scaffolds, as assessed by flow cytometry.

	Sample	Dead cells (%)	Relative live cells (%)
Control groups	Control +	76.98	-
	Control -	11.51	-
Composites	30/70	22.80	87.24
	50/50	26.42	83.15
	70/30	26.40	83.17

Figure 1

Click here to access/download;Figure;Figure 1.tif

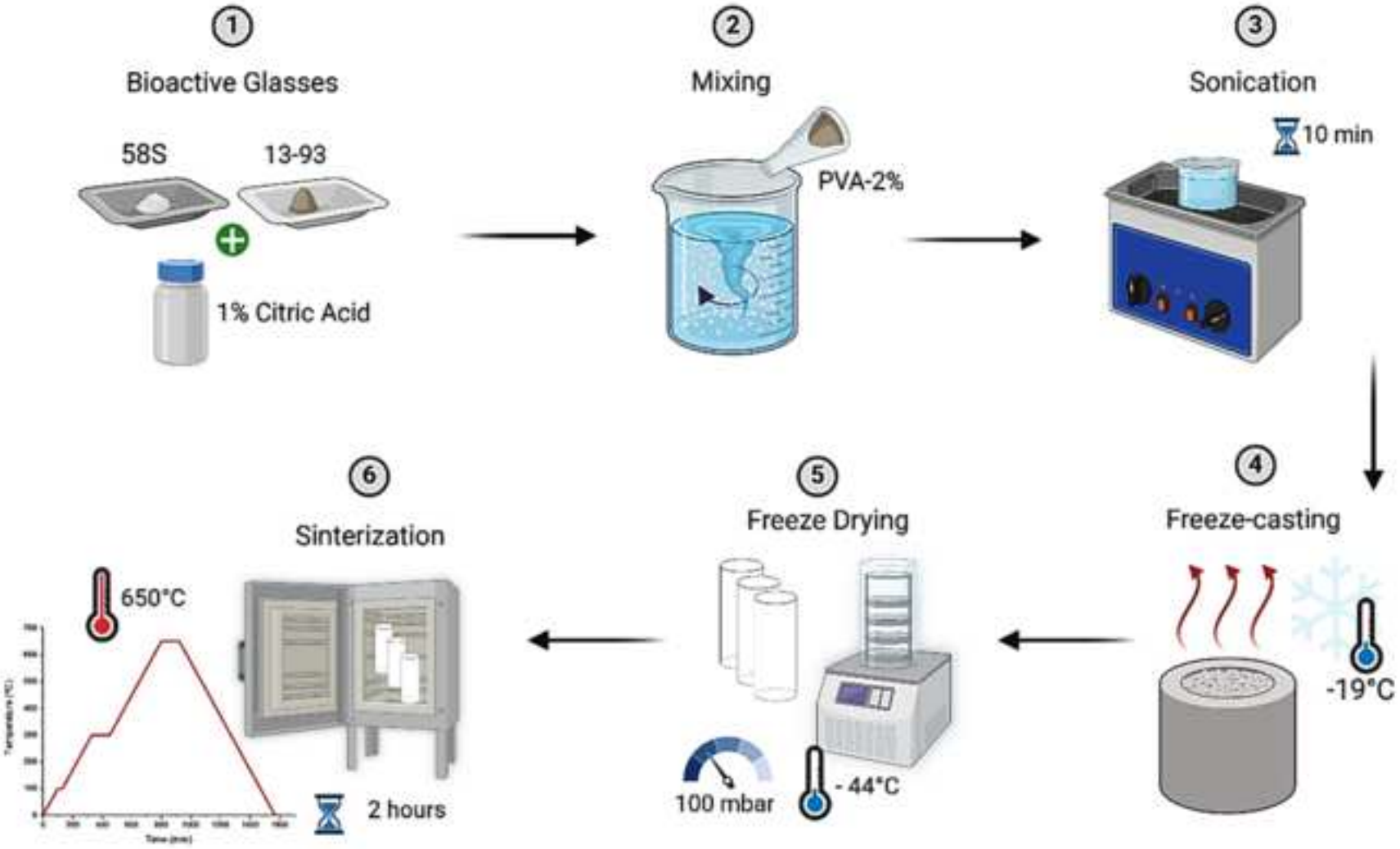

Figure 2

Click here to access/download;Figure;Figure 2.tif

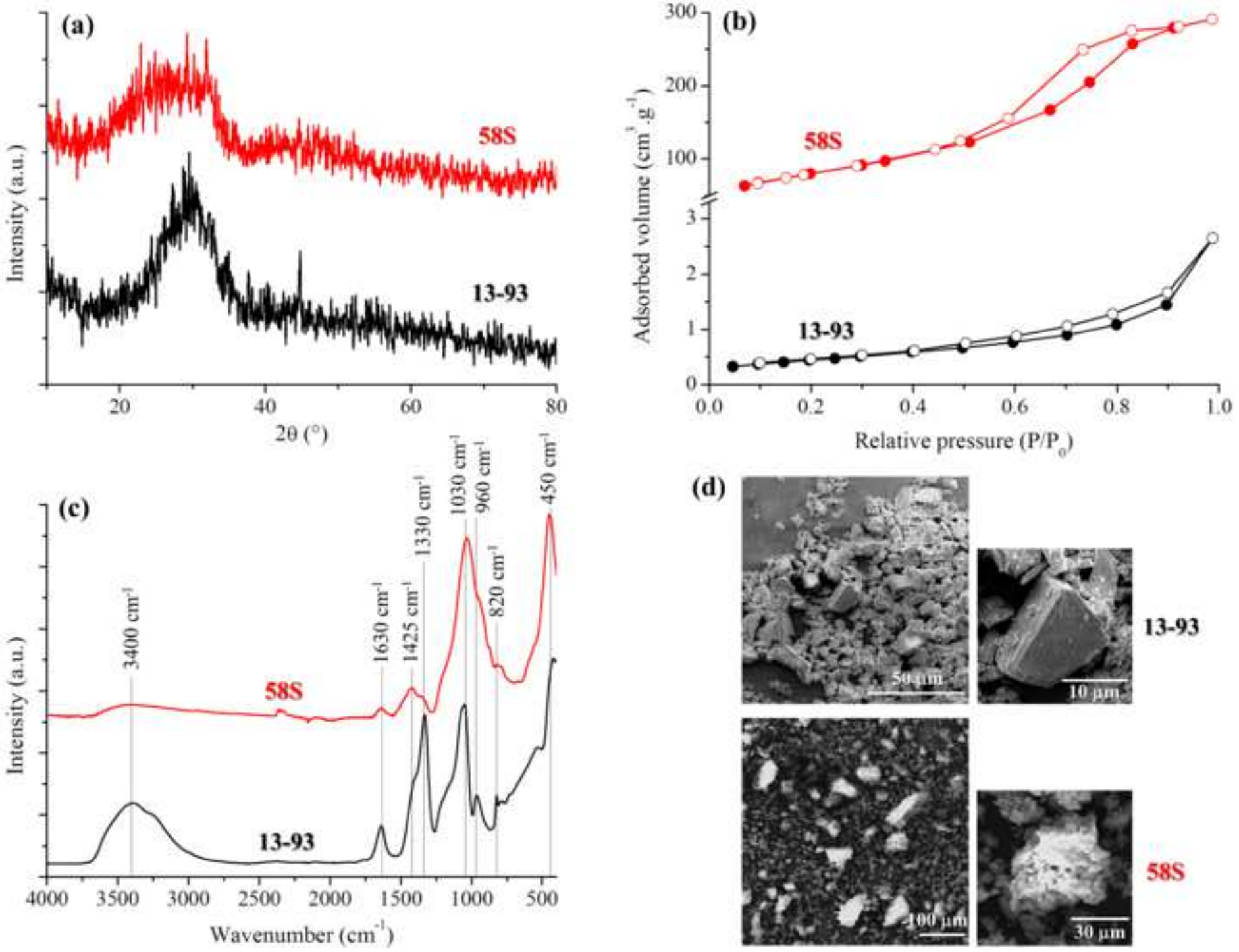

Figure 3

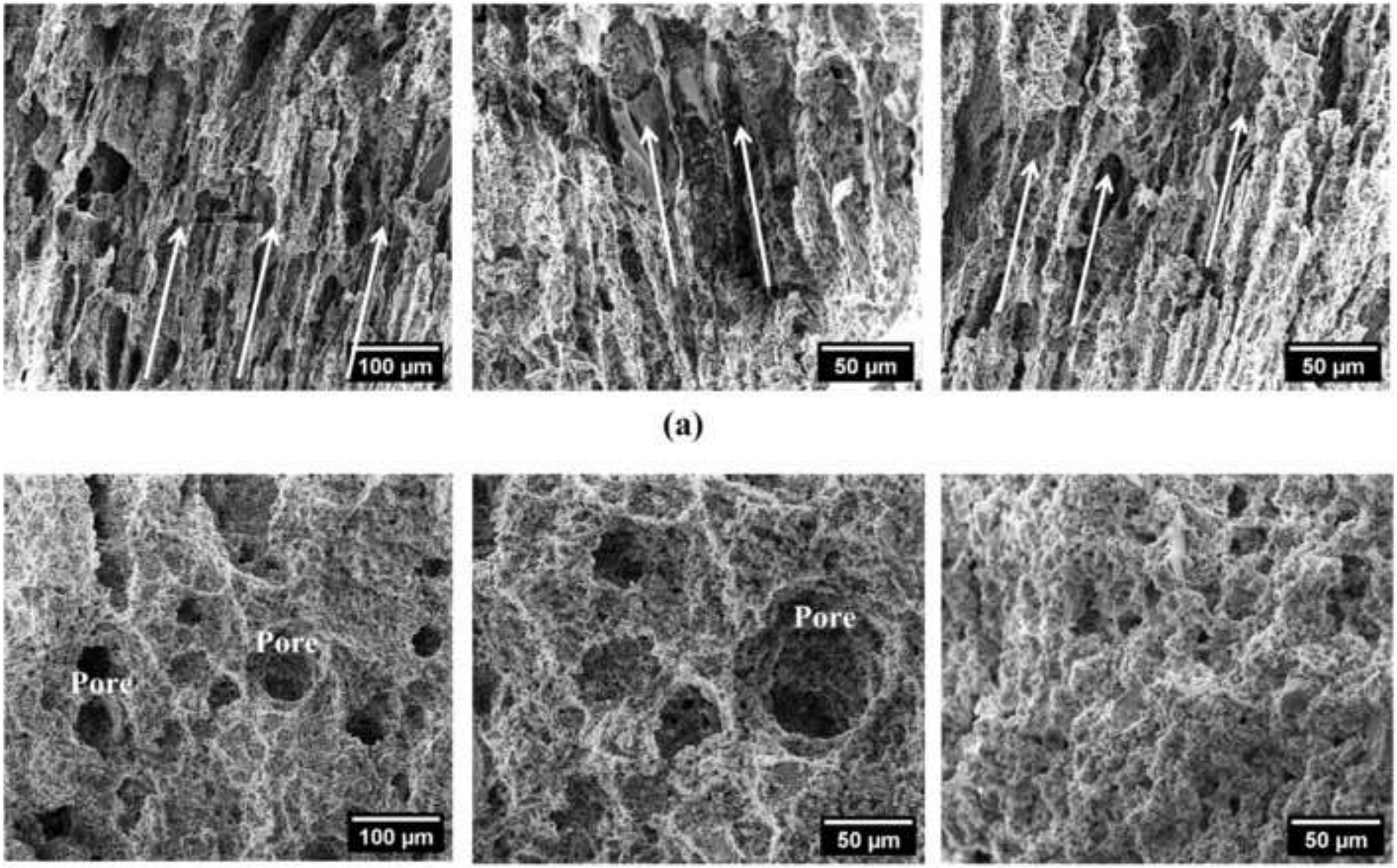

Figure 4

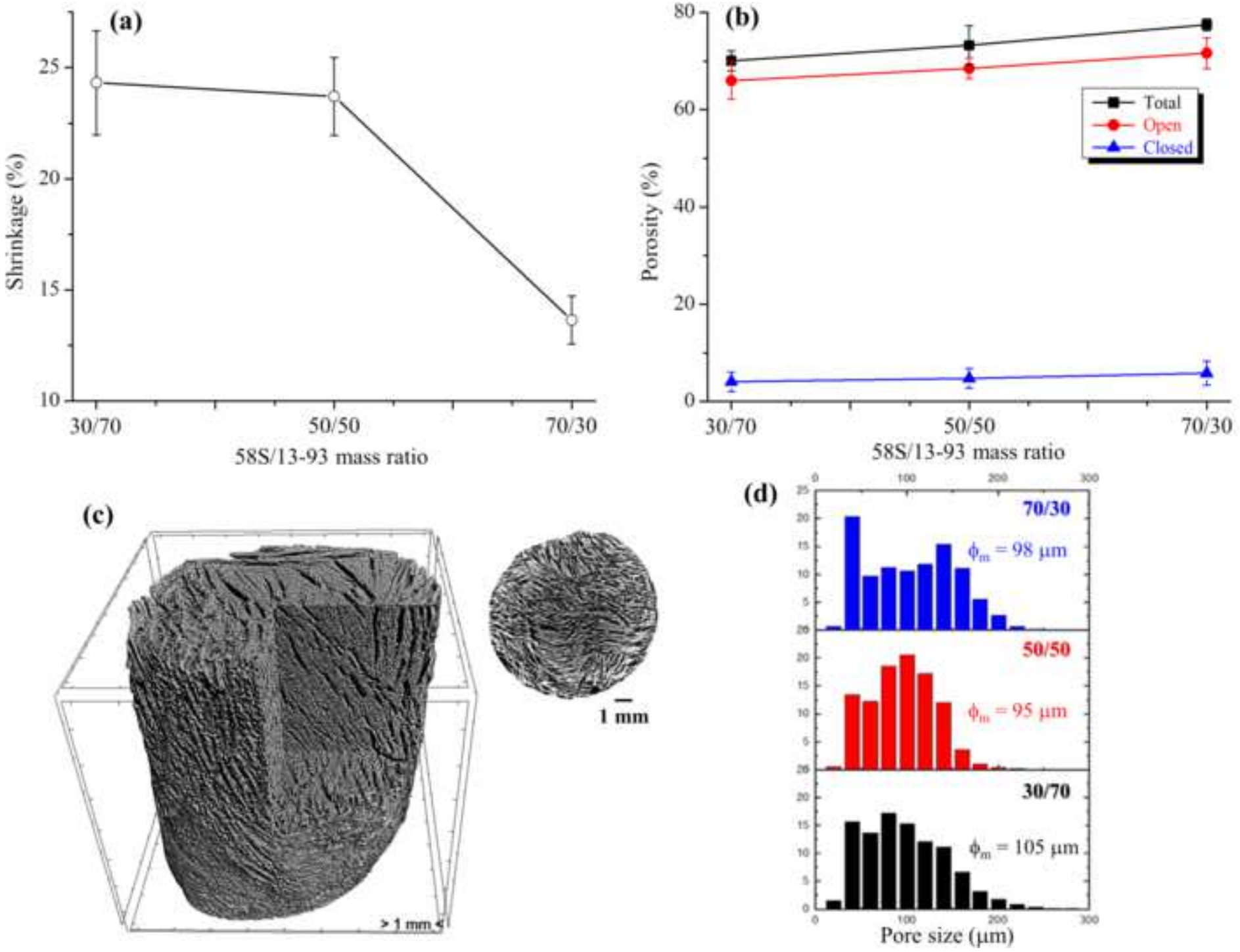

Figure 5

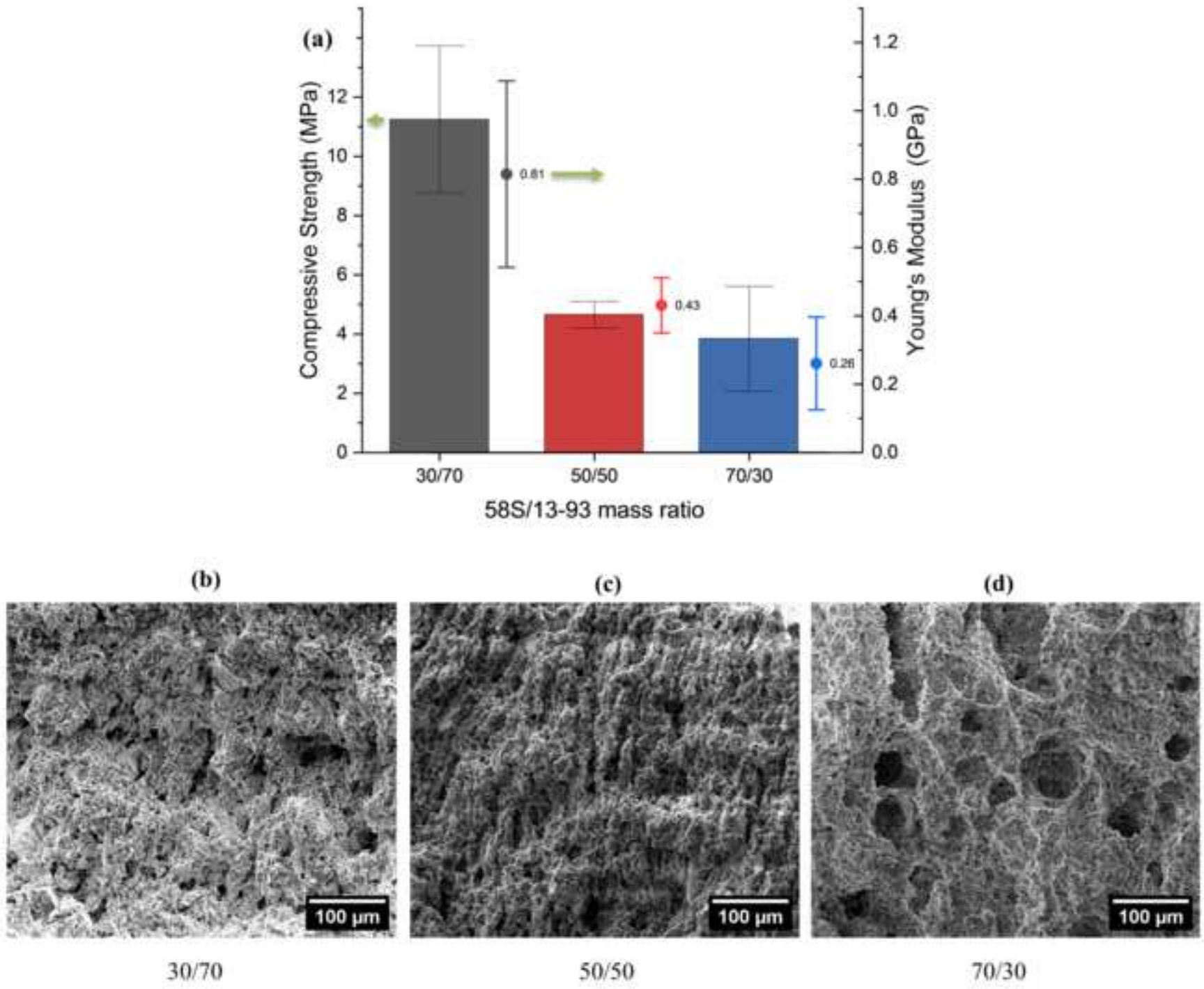

Figure 6

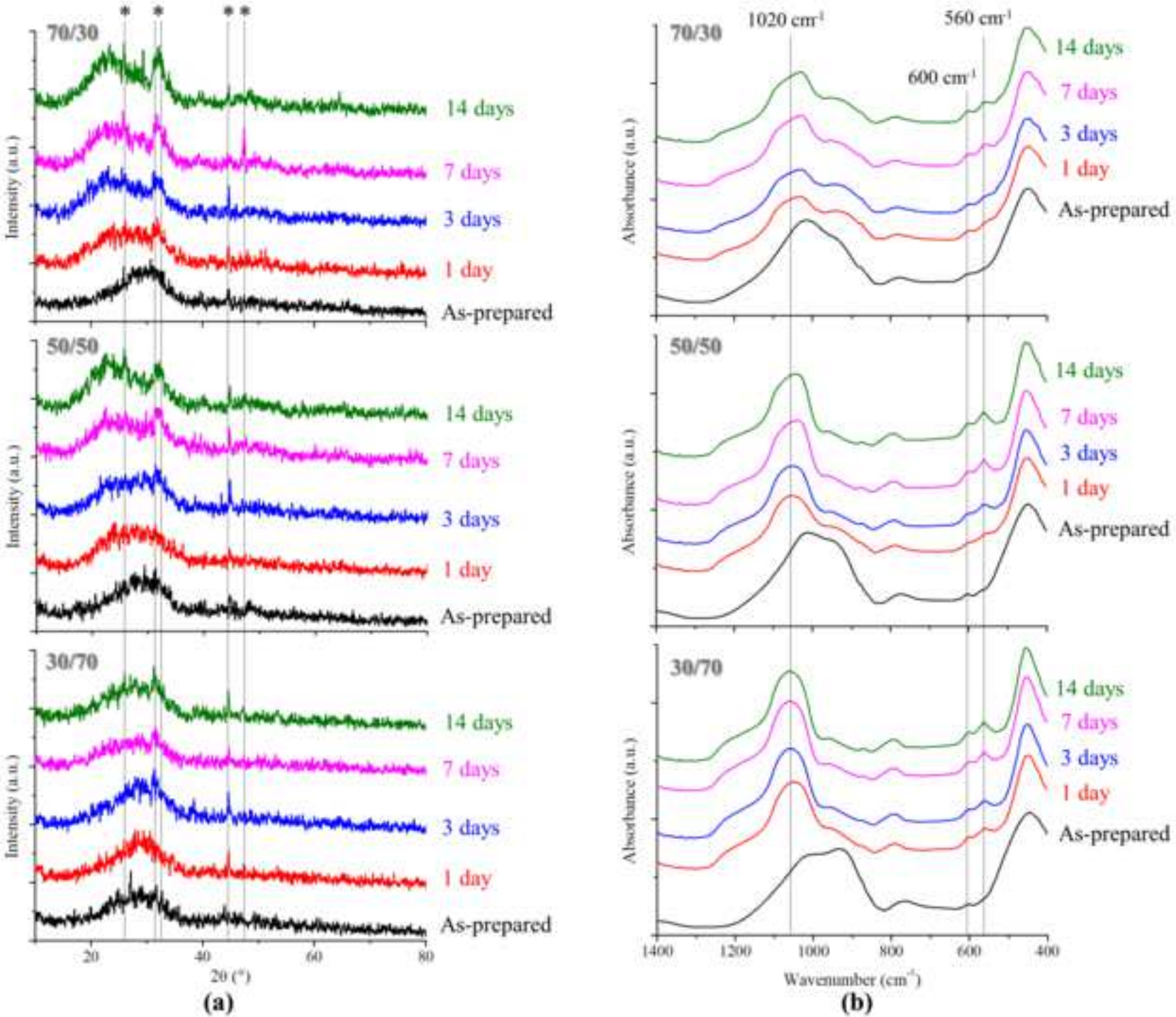

Figure 7

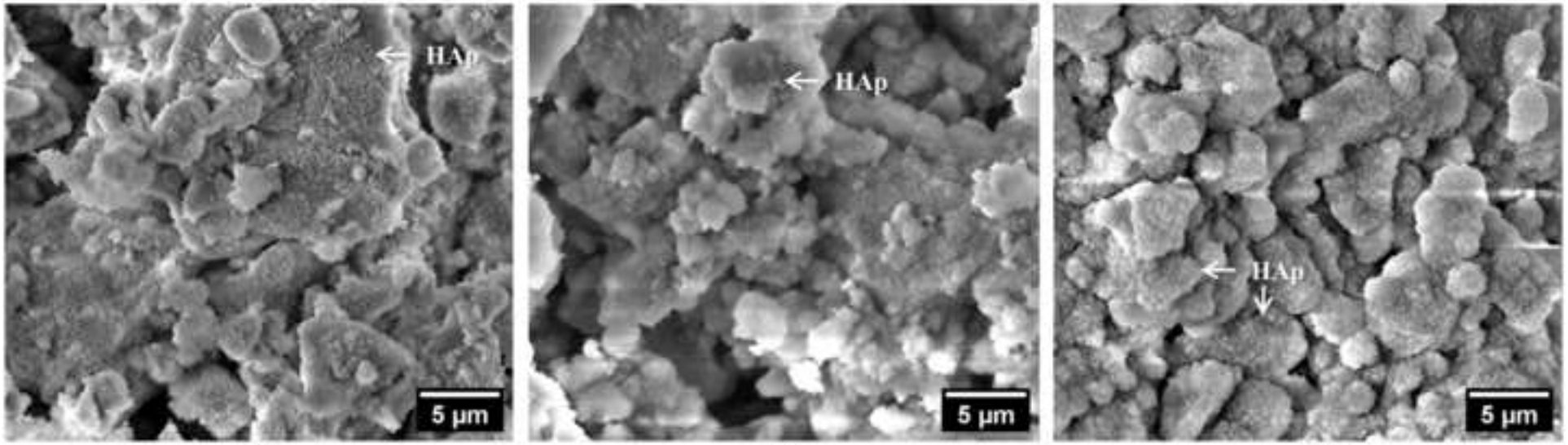

(a) (b) (c)

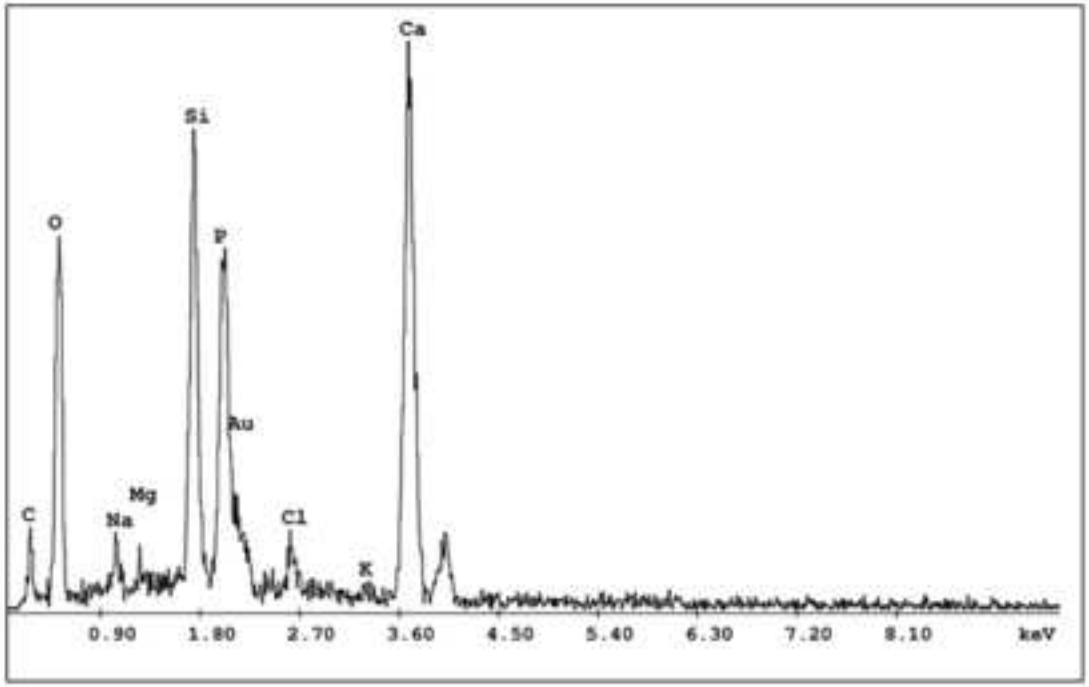

(d)

Figure 8

Click here to access/download;Figure;Figure 8.tif

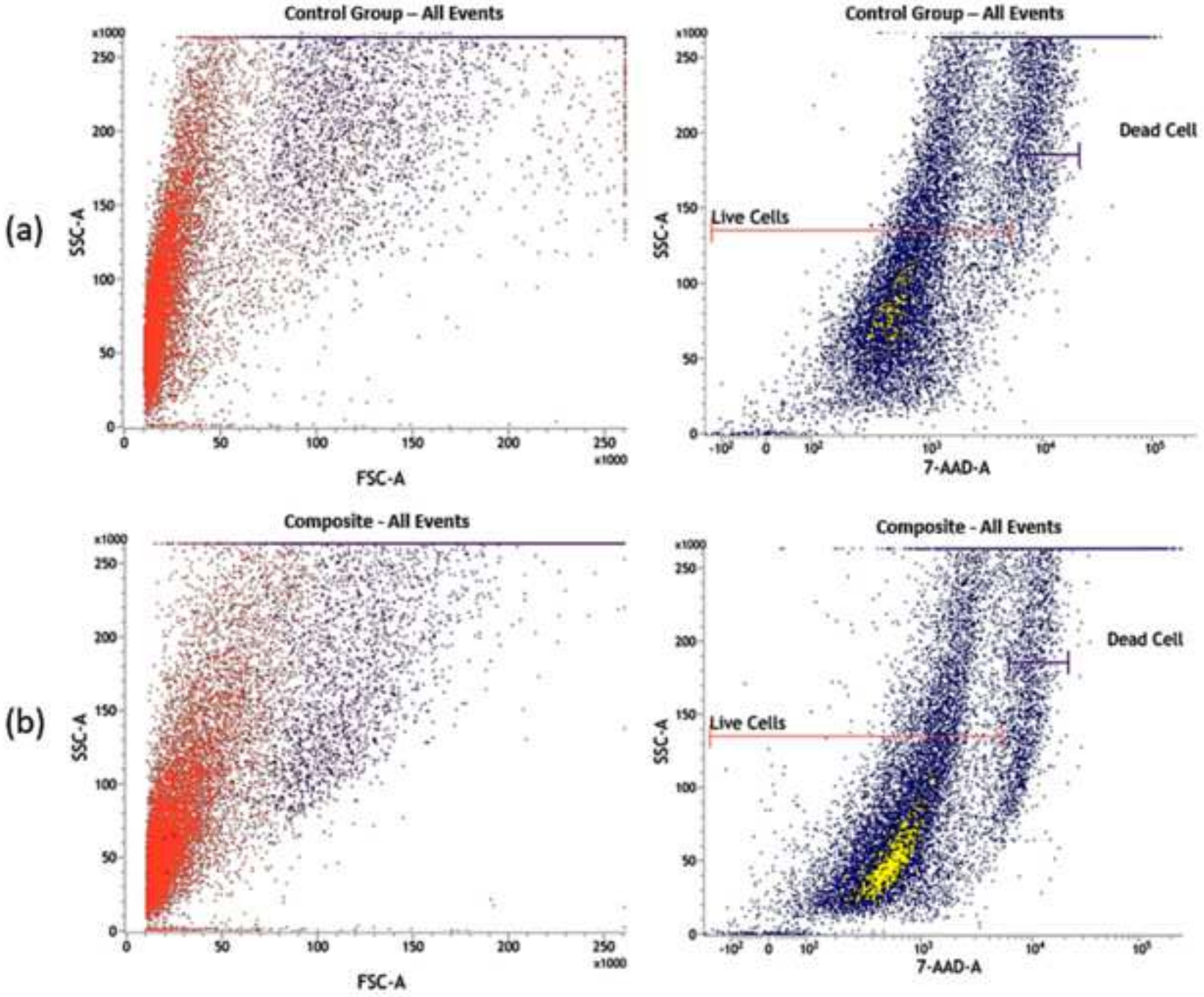

Figure 9